

Ray Tracing Algorithm for Reconfigurable Intelligent Surfaces

Sara Sandh, Hamed Radpour, Benjamin Rainer, Markus Hofer and Thomas Zemen
AIT Austrian Institute of Technology, Vienna, Austria
Email: thomas.zemen@ait.ac.at

Abstract—Ray tracing accelerated with graphics processing units (GPUs) is an accurate and efficient simulation technique of wireless communication channels. In this paper, we extend a GPU-accelerated ray tracer (RT) to support the effects of reconfigurable intelligent surfaces (RISs). To evaluate the electric field, we derived a RIS path loss model that can be integrated into a RT and enables further extensions for the implementation of additional features and incorporation into complex reflective scenarios. We verify the derivation and implementation of our model by comparison with empirical measurements in a lab environment. We demonstrate the capabilities of our model to support higher-order reflections from the RIS to the receiver. We find that such components have a significant effect on the received signal strength, concluding that the extensions of advanced functionality enabled by our model play an important role in the accurate modeling of radio wave propagation in an environment including RISs.

I. INTRODUCTION

The propagation environment in wireless communication is traditionally viewed as an uncontrollable and unpredictable system that affects the quality of the signal as it interacts with the environment. Recently, however, the concept of *smart radio environments*, that is, networks in which the environment actively assists in transferring and processing information, has emerged as a result of reconfigurable intelligent surfaces (RISs), i.e., an electronically controllable surface of electromagnetic (EM) material that can manipulate signals in real-time to constructively or destructively interfere at desired locations [1].

To achieve the full potential of RISs, several major challenges remain: real-time channel estimation, feedback of the received signal strength, control of the RIS, system optimization, and deployment, to name a few [1]. To understand the limitations and optimize configurations, it is thus of great importance to develop accurate RIS models and numerical radio wave simulation tools.

In [2] a path loss model for RIS in the millimeter wave (mmWave) frequency band is presented for an anechoic environment. Radpour et al. showed in [3] a validation with empirical measurement data using a 37 element RIS in the mmWave band that has the ability to amplify the impinging signal at each element by 3 dB using an orthogonal polarization transform [4].

For the practical use of RISs in indoor environments, the reflections of the radio signal on objects in the environment have to be taken into account. In [5] and [6], the effect of RISs

are added to a RT focusing on outdoor as well as indoor-to-outdoor scenarios. However, the higher-order reflection of the signal reflected by the RIS on other objects is not considered. In [7], RT results for a RIS are shown for a frequency band below 6 GHz, without disclosing implementation details. The authors in [8] study the usage of a RT-based RIS model in an urban scenario for a center frequency of 3.5 GHz for path loss-based system-level simulation. In [9], the authors propose a macroscopic ray-based model to compute the reradiated wave from a RIS. However, the study of a RIS-assisted RT-based model for indoor scenarios that include the reflected propagation paths between RIS and receiver (RX) is not yet available, to the best of the authors' knowledge.

Scientific contributions of this paper:

- We derive a RIS propagation model based on the ideas of [2] to compute the electric field of a RIS in complex and challenging environments.
- We implement the model within a GPU-accelerated RT [10], based on the NVIDIA OptiX ray tracing engine. The implementation is verified against empirical measurement data from [11] using a 127 element RIS.
- We demonstrate how to consider the effect of the environment that is illuminated by the RIS, including reflected paths between the RIS and the RX.

II. SIMULATION OF RECONFIGURABLE INTELLIGENT SURFACES

The RIS considered in this paper is implemented using an array of sub-wavelength patch elements that receive and re-radiate the signal with a real-time adjustable reflection coefficient, thus applying a weighting and phase shift to the reflected wave. A simplified propagation analysis of a RIS-assisted communication channel can be reduced to the following steps [12]:

- 1) Compute the emitted electric field from the transmitter (TX) towards each RIS element.
- 2) Determine the impinging field at each RIS element based on the free space path loss factor and antenna characteristics of the RIS element.
- 3) Compute the reemitted field from each RIS element towards the RX and other reflective objects in the environment using the image method.
- 4) For each reemitted component, compute the electric field at the RX.

- 5) Apply the superposition principle to obtain the total electric field at the RX.

The GPU accelerated RT considered in this paper implements a two-stage hybrid ray tracing method, combining analytic ray tracing and ray launching to model the channel characteristics as described in [10]. In the first stage, potential reflection, diffraction, and diffuse interaction points are determined analytically, without extensive validation. In the second stage, we launch rays towards the potential interaction points using the NVIDIA OptiX ray tracing engine, ensuring that only non-blocked paths are considered at the RX.

We propose an approach for the integration of RISs in our RT by launching rays towards the defined patch antenna elements. Upon intersection with the RIS, the electric field is updated according to the path loss model derived in Section II-A and relaunched as described in Section II-B.

A. Propagation Model

Starting from the path loss model in [2] that is validated with measurements from an anechoic room in [3], we generalize the far-field electric field equations for better incorporation into the RT.

We define d_y and d_z as the RIS element effective dimensions, G as the RIS element gain, and Γ_m as the complex reflection coefficient of element m . The Euclidean distance from RIS element m to the TX is d_m^t and d_m^r to the RX, as depicted in Fig. 1.

The angles of the incoming and outgoing rays are given by $(\phi_m^{e,t}, \theta_m^{e,t})$ and $(\phi_m^{e,r}, \theta_m^{e,r})$, respectively, both in relation to the coordinate system of the RIS element. Throughout this paper, elevation θ is measured from the z axis of the coordinate system in question, and azimuth ϕ from the x axis. The angle of the emitted ray from the TX and impinging wave on the RX are given by (ϕ_m^t, θ_m^t) and (ϕ_m^r, θ_m^r) , respectively, both measured from the corresponding antenna orientation matrix, as indicated in Fig. 1.

The magnitude of the directional power density (Poynting vector) can be expressed in terms of the electric field as

$$S = \frac{|\mathbf{E}|^2}{2\eta_0}, \quad (1)$$

where $\eta_0 = 120\pi \Omega$ is the impedance of free space. An electromagnetic wave emitted from an isotropic transmit antenna has the power density

$$S = \frac{P_t}{4\pi d^2} \quad (2)$$

at a distance d from the TX, with P_t denoting the transmit power.

The magnitude of the electric field emitted from a TX antenna with gain G_t and normalized radiation pattern $F_t(\phi, \theta)$, can thus be expressed as

$$|\mathbf{E}_t| = \sqrt{\frac{2\eta_0 P_t}{4\pi d^2} G_t F_t(\phi, \theta)} e^{-\frac{j2\pi d}{\lambda}}, \quad (3)$$

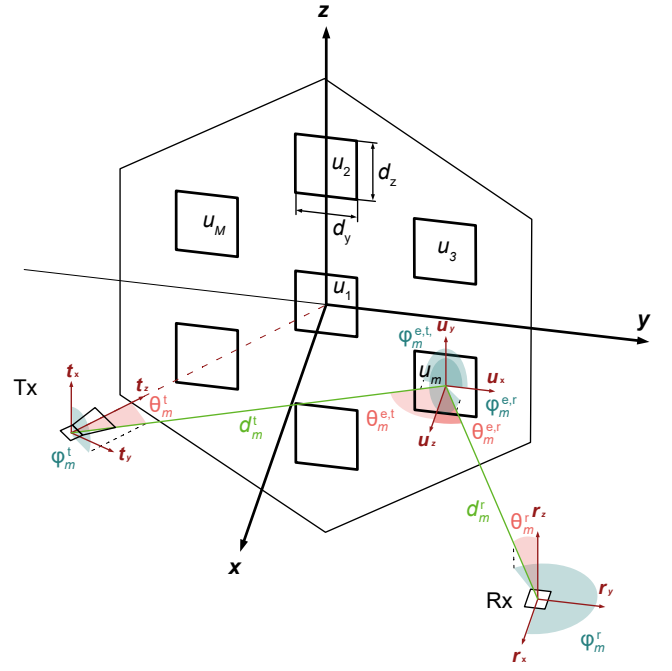


Fig. 1: Illustration of a RIS with patch elements arranged in a hexagonal grid in the yz plane. In the depicted scenario, a horn antenna at the transmitter radiates towards the center of the RIS, and a monopole RX antenna captures the signal reflected from the RIS.

where azimuth ϕ_t and elevation θ_t give the direction of the emitted field measured from the z axis of the TX antenna orientation matrix, and $\mathbf{E}_t \in \mathbb{C}^3$ is a three-dimensional complex vector describing the magnitude and polarization of the propagating electric field.

In ray tracing, the distance d is undefined until the ray hits an object or the RX. Thus, the delay and attenuation of the signal is not accounted for when computing the initial electric field at the TX. Rays launched towards the m -th RIS element center point thus have a field strength

$$|\mathbf{E}_m^t| = \sqrt{2\eta_0 P_t G_t F_t(\phi_m^t, \theta_m^t)}, \quad (4)$$

and the impinging electric field on element m is given by

$$\mathbf{E}_m^{\text{RIS,in}} = \sqrt{\frac{F(\phi_m^{e,t}, \theta_m^{e,t}) A_m}{4\pi (d_m^t)^2}} e^{-\frac{j2\pi d_m^t}{\lambda}} \mathbf{E}_m^t. \quad (5)$$

In addition to the delay and attenuation of the signal at distance d_m^t , (5) accounts for the element's normalized radiation pattern $F(\phi, \theta)$ in the direction of the impinging wave and the effective area $A_m = d_y d_z$ of the RIS element. The reemitted electric field from the m -th RIS element is given by

$$\mathbf{E}_m^{\text{RIS,out}} = \sqrt{GF(\phi_m^{e,r}, \theta_m^{e,r}) \Gamma_m} \mathbf{E}_m^{\text{RIS,in}}, \quad (6)$$

accounting for the element's gain, normalized radiation pattern, and complex reflection coefficient. Equation (6) can additionally be extended to account for the RISs effect on polarization.

TABLE I: Configuration parameters and simulation setup for RIS in a reflective environment.

Parameter	Definition
$f = 23.8$ GHz	center frequency
$P_t = 10$ dBm	TX transmit power
$G_t = 19$ dB	TX antenna gain
$G_r = 0$ dB	RX antenna gain
$\mathbf{t} = (1.86 \text{ m}, -36^\circ, 90^\circ)$	TX position in relation to RIS
$\mathbf{r} = (1.4 \text{ m}, 10^\circ, 106^\circ)$	RX position in relation to RIS
$M = 127$	number of RIS elements
$d_y, d_z = 6.6$ mm	effective RIS element size
$\Gamma_m \in \{1.25, \angle 0^\circ\}, (0, \angle 0^\circ)\}$	reflection coefficients
$\epsilon_{r,\text{metal}} = 1.0$	relative permittivity of metal
$\sigma_{\text{metal}} = 10^7 \frac{\text{S}}{\text{m}}$	conductivity of metal

A. Reflective Environment

To model the described environment in the RT, three metallic walls and a RIS object are defined, as shown in Fig. 3. Blocks of metallic material construct a $2 \times 2.4 \times 1$ m room with an opening in which a 12×12 cm RIS is placed. The RIS is centered at $\mathbf{u} = (0, 0, 0.5)$ m with surface normal $\mathbf{n} = (1, 0, 0)$. The metallic material is defined as a perfect electrical conductor (PEC) with relative permittivity $\epsilon_r = 1.0$ and conductivity $\sigma = 10^7 \frac{\text{S}}{\text{m}}$. To omit direct components from the TX to the RX, a $0.9 \times 0.05 \times 1$ m blocking panel is defined, centered at $(1.55, -0.475, 0.5)$ m in the geometry of the scene.

B. Antenna Implementation

The measurements [11] consider a TX horn antenna and a monopole RX antenna. The TX is implemented with a directional rotation symmetric antenna pattern

$$F_t(\theta) = (\cos \theta)^{\frac{G_t}{2}-1}, \quad (11)$$

with antenna gain $G_t = 19$ dB, and transmit power $P_t = 10$ dBm. The antenna orientation is set such that the main lobe at $\theta = 0$ is focused towards the RIS center point \mathbf{u} . The RX antenna is implemented with a monopole antenna model

$$F_r(\theta) = \left(\frac{\cos \frac{2\pi h}{\lambda} \cos \theta - \cos \frac{2\pi h}{\lambda}}{\sin \theta} \right)^2, \quad (12)$$

with antenna gain $G_r = 0$ dB and monopole height $h = \frac{\lambda}{4}$.

The orientation and position of the TX remain constant throughout the simulation, whereas the position of the RX is updated to sample the received signal at every position in the ranges $0.92 \leq x \leq 1.52$ m and $0.02 \leq y \leq 0.92$ m at $z = 11.4$ cm, as marked in Fig. 3, with a sampling distance of 1 cm.

C. Technical Details of the RIS

The active RISs considered in the reflective environment consists of $M = 127$ patch antenna elements with an effective element size $d_y = d_z = 6.6$ mm, arranged in a hexagonal grid. We model the normalized radiation pattern of each element as

$$F(\theta) = \cos \theta, \quad (13)$$

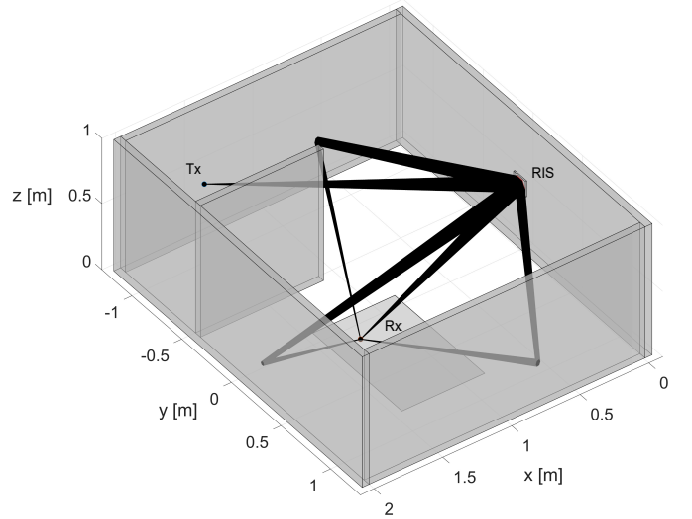


Fig. 3: Path visualization for a RIS with 127 elements in a reflection environment with the TX at $\mathbf{t} = (1.5, -1.1, 0.5)$ m, RX at $\mathbf{r} = (1.33, 0.23, 0.11)$ m, and RIS centered at $\mathbf{u} = (0, 0, 0.5)$ m.

in accordance with [2]. Each element is either switched on or off, providing an amplification of 1.25 if switched on. The reflection coefficient alphabet is thus

$$\Gamma_m \in \{1.25, \angle 0^\circ\}, (0, \angle 0^\circ)\}, \quad (14)$$

and elements are configured to optimize the received signal strength at the intended RX position according to [3, Algorithm 1].

IV. RESULTS

In this section, we validate the implemented model against measurements from [11]. Furthermore, we present the obtained results of the RT in a reflective environment by evaluating the obtained MPCs and received signal power in a simulation where reflections up to the second order from the RIS are taken into account.

A. Ray Launching

To evaluate the reflected paths between the RIS and RX, we inspect the ray launching using a path visualization tool. The simulation which did not consider higher-order reflections launch exactly one ray towards each of the 127 RIS elements. Upon intersection with the RIS, the rays are relaunched towards the RX. The simulation considering higher-order reflections additionally identify reflection points towards which rays are relaunched after intersection with the RIS, which are thereafter specularly reflected until arrival at the RX. Fig. 3 shows the generated paths from the simulation considering up to the second order reflections from the RIS for an RX placed at $\mathbf{r} = (1.33, 0.23, 0.11)$ m.

B. Received Signal Power

The measurement from [11] and equivalent RT simulations yield the received signal powers plotted in Fig. 4. The received signal power is computed and plotted for every sampling point

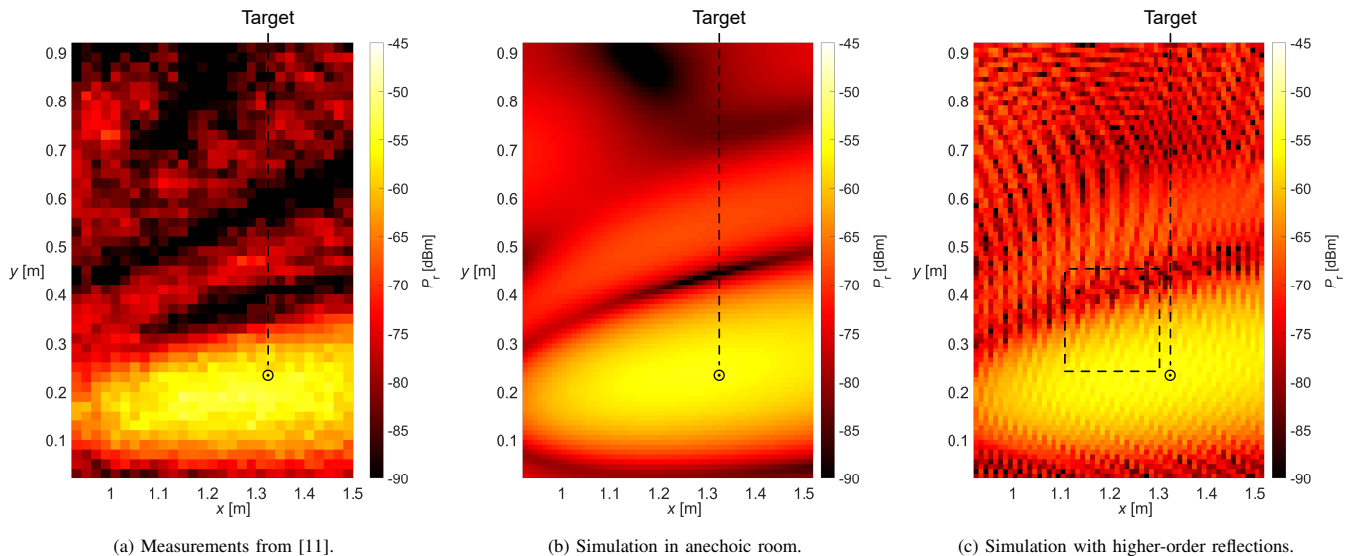


Fig. 4: Received signal power P_r from an active RIS over a region in the xy plane, measured in a lab environment from [11] in (a), simulated in an anechoic chamber (b), and simulated in a reflective environment (c). The RIS is configured to maximize the received signal at $\mathbf{r} = (1.33, 0.23, 0.11)$.

in the defined range by applying (9) and (10) to every MPC that arrives at the RX.

In Figs. 4a and 4b the signal power is plotted for the measurement in a lab environment with suppressed reflections and a simulation in an anechoic chamber, respectively. The RIS placed at $\mathbf{u} = (0, 0, 0.5)$ is configured to reflect the signal towards the RX at $\mathbf{r} = (1.33, 0.23, 0.11)$. The measured scenario shows a dominant beam of approximately 0.5×0.15 m, with a received signal power from -60 to -55 dBm, and weaker side lobes from -80 to -75 dBm. For a detailed description of the measurement results, we refer to [11]. Simulation with the RT achieves similar results, with a dominant beam centered around the RX with signal power from approximately -60 to -55 dBm over a 0.5×0.2 m region, and weaker side lobes -80 to -70 dBm.

The simulation considering reflections from the RIS up to the second order generate the plot in Fig. 4c. The constructive and destructive interference from reflected components is evident, and comparison with Fig. 4b shows that reflected propagation paths from the RIS to the RX have a large impact on the received signal strength at several locations in the considered range.

To visualize the small-scale fading pattern in more detail, we performed a high-resolution simulation of a smaller section of the xy plane, between $1.1 \leq x \leq 1.3$ m and $0.25 \leq y \leq 0.45$ m, as marked in Fig. 4c, with a sampling distance of 2 mm. The received signal power is plotted in Fig. 5, clearly showing the small-scale fading with constructive and destructive interference at approximately every $\frac{\lambda}{2}$. The reflections from the RIS can have a large impact on the received signal power, showing the importance of considering them for an accurate simulation of RISs, particularly in reflective environments.

Accurate channel descriptions are essential for the develop-

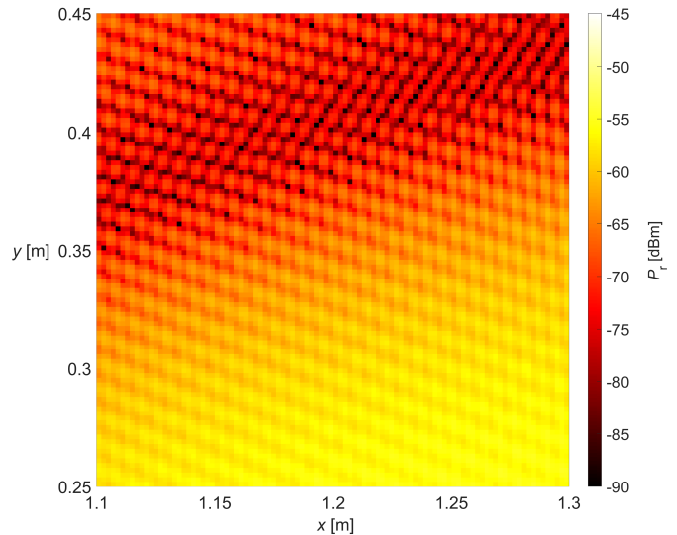


Fig. 5: High-resolution plot of received signal power P_r from a RT simulation of an active RIS in a reflective environment, considering direct and up to second order reflected signal components from the RIS.

ment of RIS control algorithms. Our RT can simulate realistic and complex environments in which reflected components from the RIS are considered, enabling the development of RIS control algorithms accounting for the small-scale fading.

V. CONCLUSION

By manipulating the signal to constructively or destructively interfere at desired locations, RISs offer promising solutions to the propagation issues for mmWaves, making it an important enabling technology for 6G wireless networks. The development of RISs require accurate models and numerical simulation tools, ray tracing being a popular technique for efficient wireless channel modeling.

In this paper, we proposed an approach for supporting the effects of RISs in complex environments by employing the image method to compute reflected paths between the RIS and the RX. For the evaluation of the electric field, we adapted the RIS path loss model proposed by Tang et al. in [2] for a GPU-accelerated ray tracer.

We validated our implementation against measurements in a lab environment from [11]. The correctness of our implementation was verified, and the model yielded reliable results for the simulated and measured case. We further evaluated the effects of a RIS in a reflective environment, showing that our model successfully enabled the extension to advanced propagation mechanisms. Furthermore, we found that higher-order reflected components from the RIS on the environment have a significant effect on the received signal strength, indicating that the extensions enabled by our model play an important role in the accurate modeling of RISs.

ACKNOWLEDGEMENT

The work of S. Sandh, H. Radpour, B. Rainer, M. Hofer and T. Zemen (corresponding author) has been funded within the Principal Scientist grant Dependable Wireless 6G Communication Systems (DEDICATE 6G) at the AIT Austrian Institute of Technology.

REFERENCES

- [1] E. Basar, M. Di Renzo, J. De Rosny, M. Debbah, M.-S. Alouini, and R. Zhang, "Wireless Communications Through Reconfigurable Intelligent Surfaces," *IEEE Access*, vol. 7, pp. 116753–116773, 2019.
- [2] W. Tang, X. Chen, M. Z. Chen, J. Y. Dai, Y. Han, M. D. Renzo, S. Jin, Q. Cheng, and T. J. Cui, "Path Loss Modeling and Measurements for Reconfigurable Intelligent Surfaces in the Millimeter-Wave Frequency Band," *IEEE Transactions on Communications*, vol. 70, no. 9, pp. 6259–6276, 2022.
- [3] H. Radpour, M. Hofer, L. W. Mayer, A. Hofmann, M. Schiefer, and T. Zemen, "Active Reconfigurable Intelligent Surface for the Millimeter-Wave Frequency Band: Design and Measurement Results," in *IEEE Wireless Communications and Networking Conference (WCNC), Dubai, United Arab Emirates*, April 2024, to be presented, online available <https://arxiv.org/abs/2306.04515>.
- [4] L. Wu, K. Lou, J. Ke, J. Liang, Z. Luo, J. Y. Dai, Q. Cheng, and T. J. Cui, "A Wideband Amplifying Reconfigurable Intelligent Surface," *IEEE Transactions on Antennas and Propagation*, vol. 70, no. 11, pp. 10623–10631, 2022.
- [5] H. Choi, J. Oh, J. Chung, G. C. Alexandropoulos, and J. Choi, "WiThRay: A Versatile Ray-Tracing Simulator for Smart Wireless Environments," *IEEE Access*, 2023.
- [6] Y. Xing, F. Vook, E. Visotsky, M. Cudak, and A. Ghosh, "Raytracing-Based System Performance of Intelligent Reflecting Surfaces at 28 GHz," in *ICC 2022-IEEE International Conference on Communications*, pp. 498–503, IEEE, 2022.
- [7] J. Huang, C.-X. Wang, Y. Sun, J. Huang, and F.-C. Zheng, "A Novel Ray Tracing Based 6G RIS Wireless Channel Model and RIS Deployment Studies in Indoor Scenarios," in *2022 IEEE 33rd Annual International Symposium on Personal, Indoor and Mobile Radio Communications (PIMRC)*, pp. 884–889, IEEE, 2022.
- [8] L. Hao, S. Schwarz, and M. Rupp, "The Extended Vienna System-Level Simulator for Reconfigurable Intelligent Surfaces," in *2023 Joint European Conference on Networks and Communications & 6G Summit (EuCNC/6G Summit)*, IEEE, 2023.
- [9] E. M. Vitucci, M. Albani, S. Kodra, M. Barbiroli, and V. Degli-Esposti, "An efficient ray-based modeling approach for scattering from reconfigurable intelligent surfaces," *IEEE Transactions on Antennas and Propagation*, 2024.
- [10] B. Rainer, D. Löschenbrand, S. Zelenbaba, M. Hofer, and T. Zemen, "Towards a Non-Stationary Correlated Fading Process for Diffuse Scattering in Ray Tracing," in *IEEE 31st Annual International Symposium on Personal, Indoor and Mobile Radio Communications*, 2020.
- [11] H. Radpour, M. Hofer, D. Löschenbrand, L. W. Mayer, A. Hofmann, M. Schiefer, and T. Zemen, "Reconfigurable Intelligent Surface for Indoor Industrial Automation: mmWave Propagation Measurement, Simulation, and Control Algorithm Requirements," in *IEEE International Symposium on Personal, Indoor and Mobile Radio Communications (PIMRC), Valencia, Spain*, September 2024, submitted, online available <https://arxiv.org/abs/2402.04844>.
- [12] E. Björnson, Ö. Özdogan, and E. G. Larsson, "Reconfigurable Intelligent Surfaces: Three Myths and Two Critical Questions," *IEEE Communications Magazine*, vol. 58, no. 12, pp. 90–96, 2020.
- [13] M. Gan, *Accurate and Low-complexity Ray Tracing Channel Modeling*. PhD thesis, Technical University of Vienna, 2015.
- [14] F. Quatresooz, S. Demey, and C. Oestges, "Tracking of Interaction Points for Improved Dynamic Ray Tracing," *IEEE Transactions on Vehicular Technology*, vol. 70, no. 7, pp. 6291–6301, 2021.
- [15] R. Collin, *Foundations for Microwave Engineering*. IEEE Press Series on Electromagnetic Wave Theory, McGraw-Hill, 1992.